33RD CONGRESS
OF THE INTERNATIONAL COUNCIL
OF THE AERONAUTICAL SCIENCES
STOCKHOLM, SWEDEN, 4-9 SEPTEMBER, 2022

ICAS 2022 SWEDEN

AERODYNAMIC AND AEROACOUSTIC CHARACTERISTICS OF THE NACA 0008 AIRFOIL

Fernanda L. dos Santos[1], Laura Botero-Bolívar[1], Cornelis H. Venner[1] & Leandro D. de Santana[1]

[1]University of Twente, Drienerlolaan 5, 7522 NB, Netherlands

Abstract

This paper discusses the flow dynamics and the leading- and trailing-edge noise generated by a NACA 0008 airfoil to better understand the near- and far-field noise characteristics of thin airfoils. Experiments were performed in the Aeroacoustic Wind Tunnel of the University of Twente for a chord-based Reynolds number ranging from 3.2×10^5 to 1×10^6. The measurements consisted of static pressure along the chord, boundary layer at the trailing edge, wall-pressure fluctuations along the chord, and far-field radiated noise. The pressure distribution along the airfoil chord, the lift coefficient, and the boundary layer characteristics at the airfoil trailing edge for different angles of attack are discussed and compared with XFOIL simulations, showing a good agreement. In case of no inflow turbulence, trailing-edge noise is dominant. The wall-pressure fluctuations at the trailing edge and the far-field noise are slightly affected by the angle of attack. At stall, the energy content of the wall-pressure fluctuations in the low-frequency range and the spanwise correlation length increase considerably. In case of inflow turbulence generated by a rod, the wall-pressure fluctuations along the airfoil chord are strongly influenced by the inflow turbulence. The highest energy content of the wall-pressure fluctuations is at chordwise positions close to the leading edge. Leading-edge noise is the dominant noise source for low- and mid-frequencies. However, trailing-edge noise level is comparable with the leading-edge noise for high frequencies.

Keywords: aerodynamic, aeroacoustic, airfoil noise, NACA0008

1. Introduction

Flow-induced noise has attracted considerable research interest in the last decades because of its importance to engineering applications and therefore for the health of people and animal life. The societal need to reduce this noise source motivated stringent regulations for radiated aeroacoustic noise [1; 2]. To comply, researchers have put great effort into understanding the generation mechanisms of flow-induced noise.

The main flow-induced noise sources are the trailing and leading edge [3]. Trailing-edge noise is generated by the scattering of turbulent structures in the boundary layer at the foil trailing edge (TE) [4]. Thus, TE noise is directly related to the wall-pressure fluctuations (WPFs) and the turbulent length scales in the boundary layer at the foil TE. This noise source is relevant for wind turbines [5], aircraft [6], and non-cavitating ship propellers [7]. TE noise is always present for a foil operating at a certain speed because this source is the minimum amount of noise produced by the foil [8]. However, for a turbulent inflow, another noise source is relevant. Leading-edge noise is generated by the interaction of turbulent inflow with a foil leading edge (LE) [9]. For the case of a foil exposed to a turbulent inflow, leading- and trailing-edge noise are competing mechanisms [10]. LE noise is dominant in the low- and mid-frequency range for applications exposed to turbulent inflow [4; 11; 10], e.g., propellers [7] and fans [12], whereas TE noise is dominant for high frequencies. Botero-Bolívar et al. [13] investigated the influence of the inflow turbulence on the WPFs at the TE of a NACA 0012. They showed that the inflow turbulence increases the WPFs at the TE, which might affect the TE noise.

The understanding of the characteristics of the near- and far-field noise is crucial for improving noise prediction models for leading- and trailing-edge noise, such as Amiet's model [9; 4]. Past studies often focused on the NACA 4-digit series foils, such as the NACA 0012 and thicker foils [14; 15; 13], due to their symmetry and relevance for helicopter rotor aeroacoustics and wind turbines. However, the thickness of foils used on ship propellers is much smaller. Thus, the knowledge of thin foils' aerodynamic and aeroacoustic characteristics is essential to this application. Also, this knowledge is important to understand the effects of thickness on noise production. Motivated by the need for a more comprehensive study on leading- and trailing-edge noise for a thin foil, the present study discusses the near-field aerodynamic and aeroacoustic characteristics as well as the far-field aeroacoustic characteristics of a NACA 0008 airfoil. The experimental measurements aim to improve the fundamental understanding of leading- and trailing-edge noise and can be used as benchmark cases for numerical and analytical studies.

2. Experimental Methodology

2.1 Wind Tunnel Facility and Airfoil Geometry

The experiments discussed in this paper were conducted in the University of Twente AeroAcoustic Wind Tunnel, an open-jet, closed-circuit facility. A centrifugal pump impulses the flow, avoiding the occurrence of wind tunnel pumping. The test section is 0.7 m $\times$ 0.9 m with a contraction ratio of 10:1. After the contraction, the flow enters a closed test section and subsequently an open test section. The experiments were performed in the open test section. The maximum operating velocity is 60 m/s in the open-jet configuration with a turbulence intensity below 0.08%. An anechoic chamber of 6 $\times$ 6 $\times$ 4 m^3 with a 160 Hz cut-off frequency encloses the test region [16]. The flow temperature was controlled at approximately 20°C. The coordinate reference system considers the downstream-direction axis x, the normal-to-the-surface direction axis y, and the spanwise direction axis z with origin at the LE mid-span; see Fig. 1.

A NACA 0008 airfoil with c = 300 mm chord and d = 700 mm span was used; see Fig. 1. The airfoil maximum thickness is 24 mm located at x/c = 0.30 and the TE thickness is t = 1 mm. The airfoil is instrumented with pressure ports along the chord and span. The pressure ports allow the measurement of the static pressure and the WPFs, which were measured using remote microphone probes (RMPs). The static pressure measurements are discussed in Section 2.2 and the WPF measurements are discussed in Section 2.5.

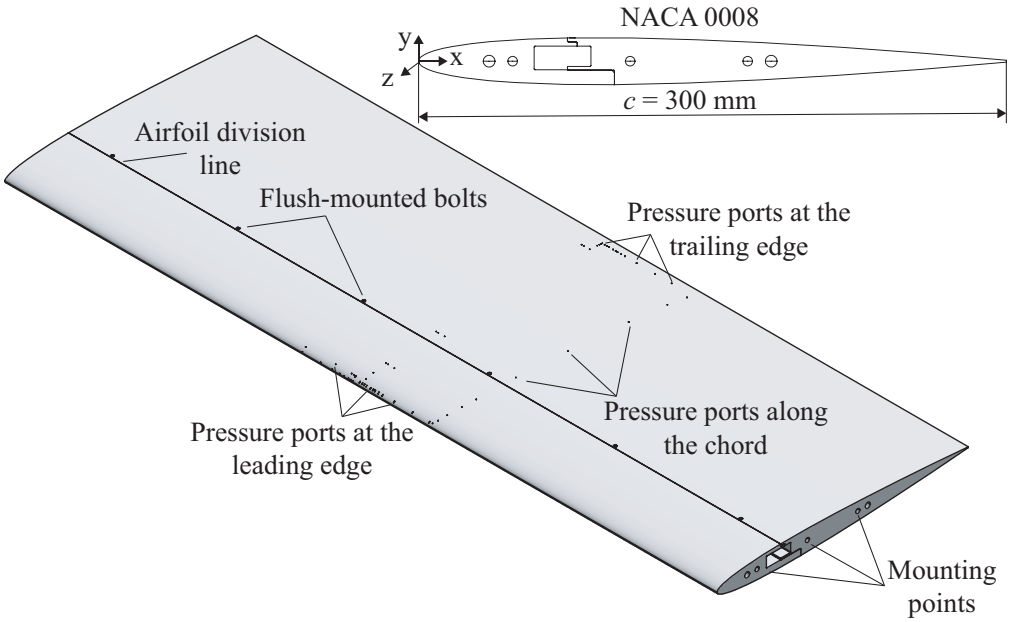

Figure 1 – Schematic view of the NACA 0008 profile with the pressure ports along the chord and spanwise direction.

2.2 Static Pressure Measurements

The static pressure was measured by the pressure ports along the chord (see Fig. 1) at 20 locations, 10 on the pressure side and 10 on the suction side, being x/c = 0.007, 0.0212, 0.05, 0.10, 0.15, 0.30, 0.50, 0.733, 0.88, 0.95. Pressure scanners (NetScanner model 9216) measured the difference between the atmospheric pressure, p_∞, and the static pressure at the airfoil surface, p. From these measurements, the pressure coefficient along the airfoil chord is calculated as:

$$C_p = \frac{p - p_\infty}{\frac{1}{2}\rho U_\infty^2} \tag{1}$$

where ρ is the fluid density and U_∞ is the free-stream velocity. U_∞ was determined from a Prandtl tube installed at the wind tunnel test section. Using the trapezoidal integration method, the lift coefficient is calculated from the measured pressure distribution.

The measurements were performed for velocities U_∞ = 10, 30, 45 m/s, resulting in chord-based Reynolds numbers of Re_c = {2,6,9}$\times 10^5$ for conditions without inflow turbulence, natural and forced transition. For forced transition, a tripping device was installed at x/c = 0.05. The height of the trip depended on the free-stream velocity, following the recommendations from dos Santos et al. [15].

2.3 Boundary Layer Measurements

The boundary layer at the airfoil TE was measured using hot-wire anemometry. A single-wire probe (Dantec Dynamics model 55P15) of 5 µm diameter and 1.25 mm wire length was used to measure the streamwise velocity. The single-wire probe was mounted in a Dantec Dynamics 55H22 probe support installed in a symmetric airfoil. This airfoil was fixed in a 3D traverse system that performed the probe translation with a resolution of 6.5 µm. The hot-wire data was acquired by the Dantec StreamLine Pro CTA system and the Dantec StreamWare software in combination with the National Instruments 9215 A/D converter. The hot-wire data was recorded for 20 s with a sampling frequency of 65,536 Hz and an anti-aliasing filter with a cut-off frequency of 30 kHz. A high-pass filter with a cut-off frequency of 5 Hz was used during the post-processing to eliminate the effect of flow buffeting instability naturally present in an open test section wind tunnel [17] which has a direct influence on the length scale calculation. The hot-wire calibration was performed in-situ in the closed test section with a Prandtl tube as reference. The calibration consisted of 32 logarithmically distributed points where the flow velocity ranged from 2.5 to 50 m/s.

The boundary layer was measured in the suction side without inflow turbulence at x/c = 0.97 and mid-span for effective angles of attack of 0°, 3° and 5°. On average, 35 points were measured inside the boundary layer and 5 points in the free stream. The y-locations of these points were spaced logarithmically. The probe's distance to the wall was determined by the contact of a feeler gauge to the hot-wire prongs. The gauge accuracy is 0.05 mm. Also, the measurements were performed for velocities U_∞ = 10, 30, 45 m/s (Re_c = {2,6,9}$\times 10^5$). The boundary layer was measured for natural transition and forced transition at x/c = 0.05. For Re_c = 6$\times 10^5$, a trip height of 0.3 mm was used for effective angles of attack α_{eff} = 0° and 3°, and a trip height of 0.6 mm was used for α_{eff} = 5°. These trip heights were chosen following the recommendations of dos Santos et al. [15].

2.4 Inflow Turbulence

To evaluate the LE near-field and the LE far-field noise generated by the NACA 0008 airfoil, WPFs and far-field noise measurements were performed when the airfoil was subjected to inflow turbulence. This turbulence was generated by a rod of 40 mm diameter; see Fig. 2. The rod was installed 1 m upstream of the airfoil LE. The width of the wake generated by the rod at the LE position (at x = 0) is approximately 20 times larger than the airfoil maximum thickness. The turbulence characteristics of the rod were measured by hot-wire anemometry. Table 1 lists the turbulence parameters for the wake of the rod at the LE location with the airfoil removed, where Re_d is the Reynolds number based on the rod diameter, u_{rms} is the root-mean-square of the velocity fluctuations, and Λ_f is the turbulence longitudinal integral length scale. More information about the generated inflow turbulence can be found in [18].

Table 1 – Turbulence parameters generated by the rod at the LE position with the airfoil removed.

Re_c [-]	Re_d [-]	u_{rms} [m/s]	Λ_f [mm]
3.2×10^5	4.3×10^4	3.08	60.0
4.0×10^5	5.3×10^4	3.81	68.9
4.8×10^5	6.4×10^4	4.55	72.9
5.6×10^5	7.5×10^4	5.16	80.6
6.4×10^5	8.5×10^4	5.87	90.5
7.2×10^5	9.6×10^4	6.49	92.2
7.9×10^5	1.1×10^5	7.13	101
-	-	-	-

2.5 Wall-Pressure Fluctuation and Far-Field Noise Measurements

The WPFs were measured using the RMP technique using 82 microphones (FG-23329-P07 Knowles). More information about this technique can be found in [19; 20]. The measurements without inflow turbulence were performed for U_∞ = 20:5:45 m/s (Re_c = {2, 3, 4, 5, 6, 7, 8, 9}$\times 10^5$) for α_{eff} = 0°, 3°, 5°, and at stall. With inflow turbulence, the measurements were performed for Re_c = {3.2,4.8,6.4}$\times 10^5$ at zero angle of attack. More information about the WPF measurement setup and the calibration used in this study can be found in [18].

A microphone phased array was used to localize and quantify the trailing- and leading-edge noise generated by the NACA 0008. A circular array with a 1 m diameter consisting of 62 GRAS 40 PH microphones distributed in a Vogel spiral arrangement was used; see Fig. 2. This array geometry yields a flat mainlobe-to-sidelobe ratio (MSR) in a wide frequency range [21]. The sensitivity of each microphone was calibrated using the pistonphone GRAS 42AG Multifunction Sound Calibrator with a sound pressure level of 94 dB and frequency of 1 kHz. The microphone array plane was parallel to the plane composed of the airfoil chord-span lines at a zero angle of attack. The distance between the microphone array and the airfoil was 1.5 m. The array center was aligned with the airfoil center.

The WPFs and the far-field noise were acquired at a sampling frequency of 65,536 Hz using PXIe-4499 Sound and Vibration modules installed in a NI PXIe-1073 chassis. The acquisition time was 30 seconds.

2.5.1 Noise Source Estimation

The noise localization and quantification were performed using an in-house beamforming code benchmarked against an array benchmark database [22; 23]. The cross-spectral matrix (CSM) was estimated using Welch's method with parameters described in Section 2.6. Diagonal removal was applied to the cross-spectral matrix. Microphone weighting was not applied in the beamforming process. The frequency response of each microphone was accounted for within the CSM calculation. Conventional beamforming in the frequency domain was performed on a searching grid ranging x/c = [-2,3] and z/d = [-0.71,0.71] in the plane composed of the airfoil chord-span lines. The grid resolution was 30 mm.

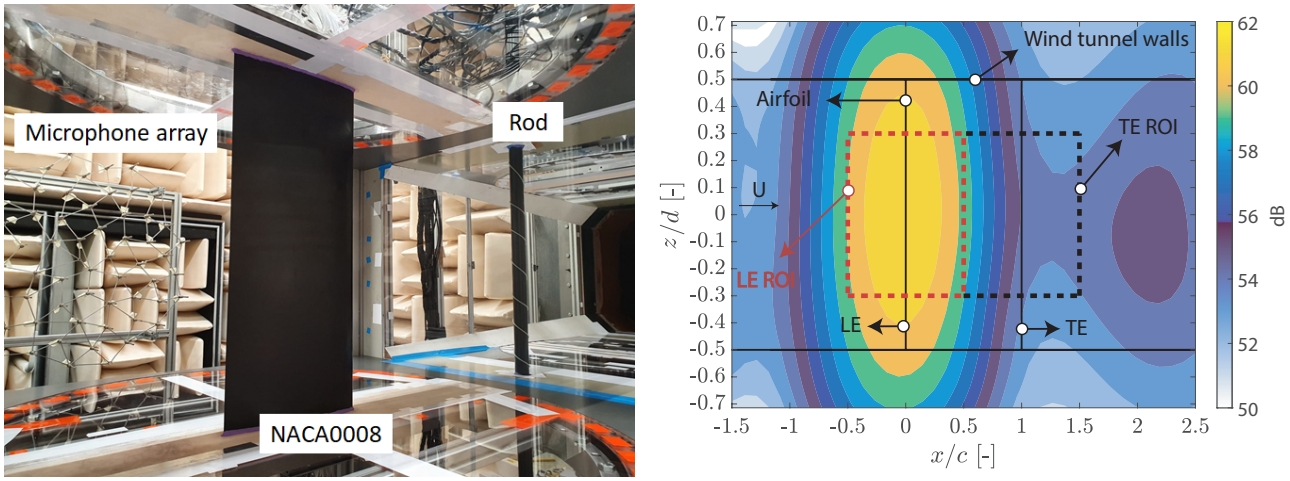

Figure 2 – Experimental setup (a), and source map (b) for 1/3-octave band with center frequency of 1,587 Hz for Re_c = 4.8$\times 10^5$ with the rod generating the inflow turbulence.

Trailing-edge noise estimation
TE noise was measured for the condition where no body was generating inflow turbulence for free-stream velocities U_∞ = 20:5:50 m/s (Re_c = {4, 5, 6, 7, 8, 9, 10}$\times 10^5$). Tripping devices were used to hasten the laminar-turbulent transition to ensure that the boundary layer at the TE was turbulent. The trip height depended on the tested velocity, following the recommendations of dos Santos et al. [15]. The TE noise radiated by the airfoil was determined with the source power integration (SPI) technique [24]. The region of integration (ROI) was x/c = [0.5, 1.5] and z/d = [-0.3, 0.3]; see Fig. 2. The power spectral density (PSD) of the SPI is given at the array center. The uncertainty of the sound power estimated by conventional beamforming in the frequency domain method is around 1 dB [23].

Leading-edge noise estimation
LE noise was measured for the inflow turbulence generated by a rod for free-stream velocities U_∞ = 16, 20, 24, 28, 32, 36, 39 m/s (Re_c = {3.2, 4.0, 4.8, 5.6, 6.4, 7.2, 7.9}$\times 10^5$). This noise source was isolated with the SPI technique. The ROI was x/c = [-0.5, 0.5] and z/d = [-0.3, 0.3]; see Fig. 2. The PSD from the SPI is given at the array center.

2.6 Spectrum Determination
The PSD of the WPFs, Φ_{pp}, and the CSM were calculated using Welch's method. The data was averaged using blocks of 8192 samples (125 ms) and windowed by a Hanning windowing function with 50% overlap, resulting in a frequency resolution of 8 Hz. The spectral levels are shown in dB, calculated as in Eq. 8.4.8 in [3]. For Φ_{pp}, the reference values were p_{ref} = 1 Pa and Δf_{ref} = 1 Hz, whereas for the far-field noise they were p_{ref} = 20 μPa and Δf_{ref} = 1 Hz.

3. Aerodynamic Characterization
In this section, the pressure distribution along the airfoil chord and the boundary layer parameters at the airfoil TE are discussed. The measurements are compared with XFOIL simulations because of its short turn-around time, making this tool ideal for design and optimization processes. Also, XFOIL is a valuable tool when used in combination with Amiet's theory [4] coupled with a wall-pressure spectrum model [25; 26; 27] to estimate the TE far-field noise [13; 28]. First, the XFOIL simulations are addressed. Subsequently, the pressure distribution and the lift coefficient measured are compared with XFOIL results. Finally, the boundary layer parameters at the airfoil TE obtained from hot-wire measurements are discussed and compared with the values from XFOIL.

3.1 XFOIL Simulations
XFOIL simulations [29] were performed to obtain the pressure distribution, the lift coefficient, and the boundary layer parameters at the airfoil TE. The input parameters for XFOIL were the chord-based Reynolds number, Re_c, Mach number, M, the effective angle of attack, α_{eff}, and the transition position, which could be natural transition or forced transition at x/c = 0.05. The input values depended on the measurement condition that was compared with XFOIL. The input values are specified for each comparison made in the following sections. The speed of sound was 343 m/s.
The pressure distribution is a direct output of XFOIL, which is given as the pressure coefficient, C_p. The boundary layer shape factor, H, displacement thickness, δ^*, and momentum thickness, θ, at different chord positions are also outputs of XFOIL. XFOIL also computes the lift coefficient, C_l. The boundary layer thickness can be calculated from δ^* and θ, given as [30]:

$$\delta(x) = \theta(x)\left(3.15 + \frac{1.72}{H_k(x)-1} + \delta^*(x)\right) \tag{2}$$

where H_k is the boundary layer kinematic shape parameter [30]:

$$H_k(x) = \frac{H(x) - 0.290M_e^2}{1 + 0.113M_e^2} \tag{3}$$

where M_e is the Mach number based on the boundary layer edge velocity. For low Mach number flows, H_k reduces to the shape factor $H = \delta^*/\theta$. This approximation was used in this study. The boundary layer thickness is computed at x/c = 0.97 because this is the position where the hot-wire measurements were performed.

3.2 Pressure Distribution and Lift Coefficient

Figure 3 shows the comparison between the measured and the XFOIL simulated pressure distributions for different effective angles of attack, Re_c = 6×10^5 and forced transition at x/c = 0.05. The effective angle of attack is determined from the wind tunnel correction given in [31]. For α_{eff} = 0°, there is a good agreement between the measured and simulated C_p, except for the suction side for positions close to the LE. This might be because the airfoil is not exactly at zero angle of attack. This is also noticed in the lift curves (see Fig. 4) where a small amount of lift is generated for α_{eff} = 0°. For α_{eff} = 3°, the C_p measured is higher than the simulated in the suction side and lower in the pressure side, indicating that the airfoil generates more lift than the simulated by XFOIL. This is confirmed from the C_l curves (see Fig. 4). For $\alpha_{\text{eff}} \geq$6°, a good agreement between the C_p measured and simulated is observed for $x/c >$0.4. However, the measurements do not capture the suction peak precisely. This mismatch might be due to the effective angle of attack estimation, which becomes more relevant for high angles of attack. Similar findings were observed for the other Reynolds numbers tested.

Figure 4 compares the experimental and the simulated lift coefficients as a function of α_{eff} for the cases of forced and natural transitions. A good agreement between the experimental and the simulated curves is observed for small angles of attack ($\alpha_{\text{eff}} < 3°$). The experimental and the simulated curves have a better match for high angles of attack as the Reynolds number increases. Also, the curves seem to have a Reynolds number dependency, mainly for the forced transition case.

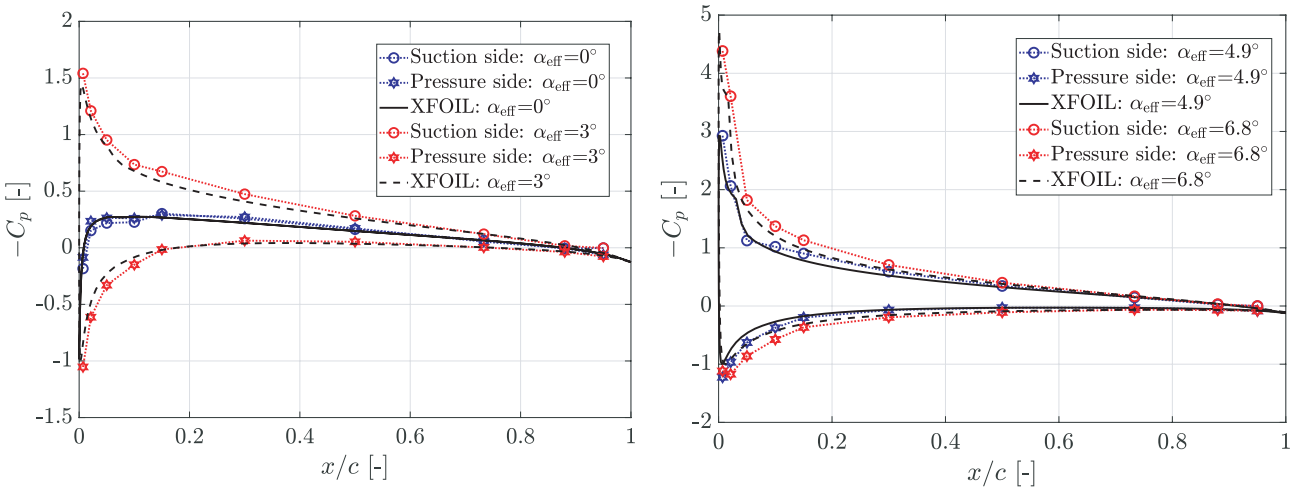

Figure 3 – Comparison between the measured and the XFOIL simulated pressure distributions for Re_c = 6×10^5 and M = 0.087 for forced transition at x/c = 0.05.

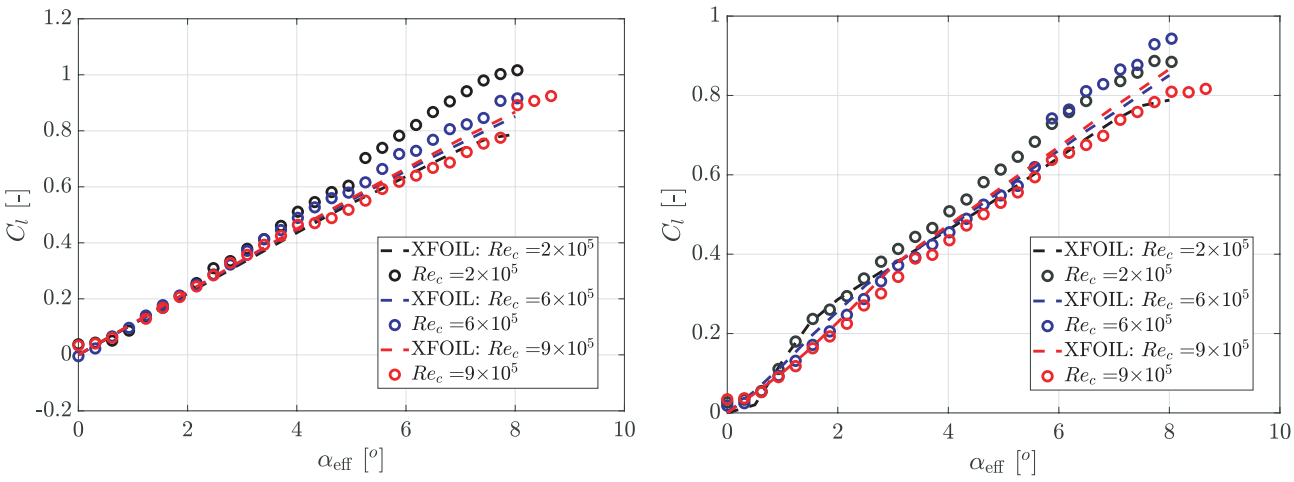

(a) Forced transition at x/c = 0.05

(b) Natural transition

Figure 4 – Comparison between the experimental and the XFOIL simulated C_l for different Reynolds numbers. Two cases are shown: forced transition and natural transition.

3.3 Boundary Layer at the Airfoil Trailing Edge

Figure 5 shows the velocity and the turbulence intensity profiles at x/c = 0.97 in the suction side for forced transition at x/c = 0.05 for different effective angles of attack. The velocity profile measured is fitted to the law of the wall using the equation proposed by Coles [32]. The friction velocity, u_τ, is determined from this fitting. The angle of attack directly affects the velocity and the turbulence intensity profiles, resulting in higher turbulence intensities as the angle of attack increases. The fitted law-of-the-wall equation can accurately represent the velocity profile for the different angles of attack. Furthermore, the friction velocity decreases as the angle of attack increases.

The boundary layer thickness is determined as the distance from the wall where the velocity corresponds to 99% of the edge velocity, U_e. The boundary layer displacement and momentum thicknesses, δ^* and θ, respectively, are determined from the integration of the measured boundary layer velocity profile. Table 2 shows the experimental and simulated boundary layer parameters for different angles of attack for Re_c = 6×10^5. By increasing the angle of attack, the TE boundary layer on the suction side becomes thicker. The increase of the boundary layer thickness is due to the stronger adverse pressure gradient that the airfoil is subjected to because of the higher angle of attack. The same tendency is also observed for the XFOIL simulations. These simulations predict δ, δ^*, and θ with an error up to 32%, which is satisfactory since many factors influence the boundary layer thickness measured, such as the tripping device used [15]. Dos Santos et al. [15] showed that the boundary layer thickness varies significantly with the trip height used. They showed that δ increased 35% as the trip height increased, even though the trip height used was smaller than the boundary layer thickness at the trip location. The agreement between the simulation and the measurement improves for higher angles of attack. The agreement of the experimental and simulated friction velocity is good for $\alpha_{\text{eff}} \leq 3°$, but it worsens as the angle of attack increases. Similar results were observed for the other Reynolds numbers tested.

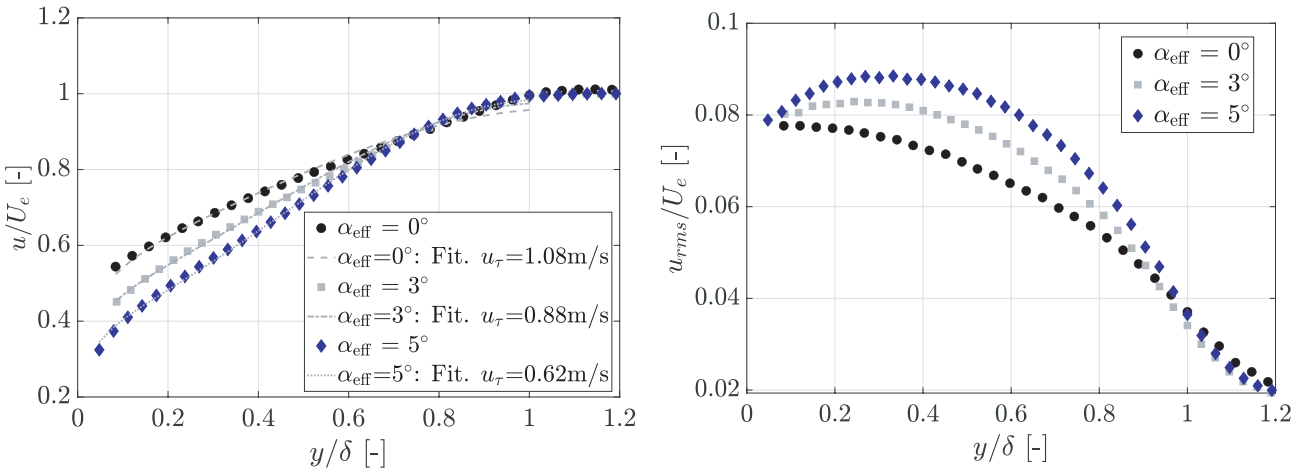

(a) Velocity profile

(b) Turbulence intensity profile

Figure 5 – Boundary layer velocity and turbulence intensity profiles at x/c = 0.97 in the suction side for Re_c = 6×10^5 and for different effective angles of attack.

Table 2 – Boundary layer parameters at x/c = 0.97 for different effective angles of attack for Re_c = 6×10^5. The values between curly brackets correspond to the boundary layer parameters for $\alpha_{\text{eff}} = \{0°, 3°, 5°\}$.

	δ [mm]	δ^* [mm]	θ [mm]	u_τ [ms/]
Experiment	{6.0, 8.1, 10.4}	{1.1, 1.8, 2.8}	{0.8, 1.2, 1.6}	{1.08, 0.88, 0.62}
XFOIL	{4.4, 7.2, 10.1}	{0.8, 1.5, 2.3}	{0.5, 1.0, 1.4}	{1.17,0.98,0.91}
$\frac{\lvert\text{Exp.}-\text{XFOIL}\rvert}{\text{Exp.}}$	{27%,11%,3%}	{26%,12%,18%}	{32%,18%,16%}	{8%,12%,46%}

4. Aeroacoustic Characterization

In this section, the WPFs and the leading- and trailing-edge noise measured are discussed. Initially, the WPFs for the cases with and without inflow turbulence are addressed. Subsequently, the leading- and trailing-edge noise are analyzed. A comparison of these two noise sources is also included at the end of this section.

4.1 Wall-Pressure Fluctuation Spectrum and Spanwise Correlation Length

Figure 6 shows the PSD of the WPFs, Φ_{pp}, at x/c = 0.97 for different Reynolds numbers, α_{eff} = 0° and no inflow turbulence. As expected, the WPF spectral level increases as the Reynolds number increases. The scaling of the WPFs with the free-stream velocity is verified in Fig. 6b. The x-axis is shown as the Strouhal number based on the boundary layer thickness at the TE determined from XFOIL. The measured boundary layer thickness is not used because we have not measured it for all the free-stream velocities shown in Fig. 6. As can be seen from this figure, the WPF level scales with the velocity to the power two.

Figure 7 shows the PSD of the WPFs, Φ_{pp}, and the spanwise correlation length, l_y, at x/c = 0.97 for different angles of attack for the case without inflow turbulence. The spanwise correlation length was calculated as discussed in [18]. The WPF spectral level increases for low frequencies as the angle of attack increases. This behavior indicates that larger turbulent structures contain more energy for higher angles of attack. The correlation length also increases as the angle of attack increases. The increase of l_y is because the boundary layer at the TE on the suction side becomes thicker for higher angles of attack (see Table 2), increasing the turbulence length scales inside the boundary layer. This occurs because the large structures in the boundary layer are on the order of magnitude of the boundary layer thickness [3]. At stall, i.e., α_{eff} = 11°, a significant increase of the energy content is observed in the low-frequency range. This growth is associated with the large vortices formed when the flow is separated. This observation is supported by the spanwise correlation length results, also shown in Fig. 7, where a considerable increase of the correlation length is observed for low frequencies.

The WPFs are also evaluated for the case of inflow turbulence. Figure 8 shows the WPF spectrum for different chordwise positions. The highest energy level is observed at x/c = 0.007, as expected, since this position is the closest to the LE, interacting directly with the inflow turbulence. A hump is observed in the low-frequency range, probably caused by the rod vortex shedding interacting with the airfoil LE. This hump is clearly seen up to x/c = 0.73, showing that the inflow turbulence affects the WPFs in the low-frequency range, as also discussed by Botero-Bolivar et al. [13]. Figure 8 also shows that the spanwise correlation length decreases in the chordwise direction. These results were also observed for the other Reynolds numbers tested.

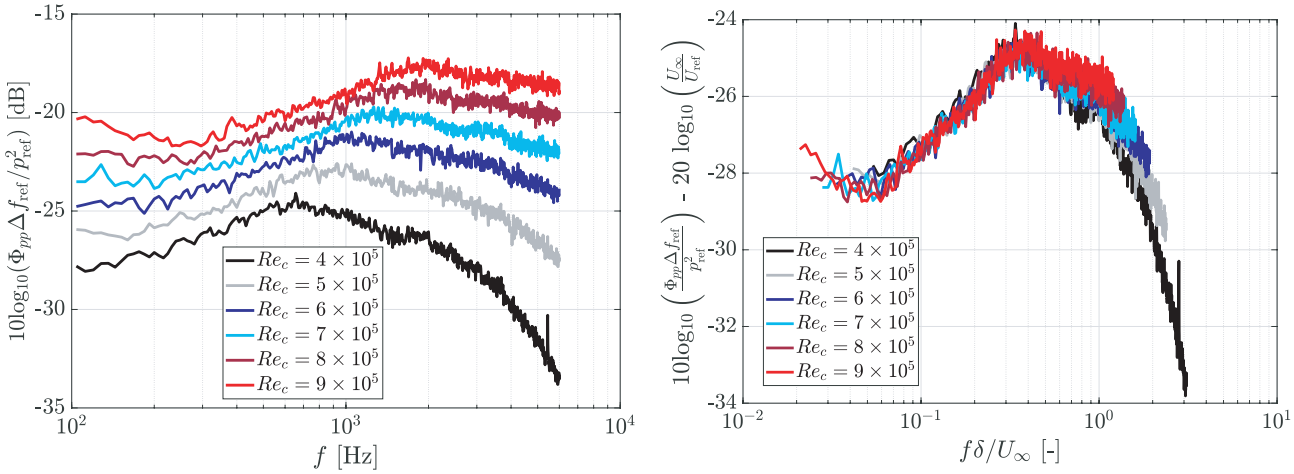

(a) Dimensional

(b) Level scaling: U_∞^2

Figure 6 – PSD of the WPFs at x/c = 0.97 in the suction side for different Reynolds numbers, α_{eff} = 0° and no inflow turbulence. Reference values: p_{ref} = 1 Pa, Δf_{ref} = 1 Hz, U_∞ = 20 m/s.

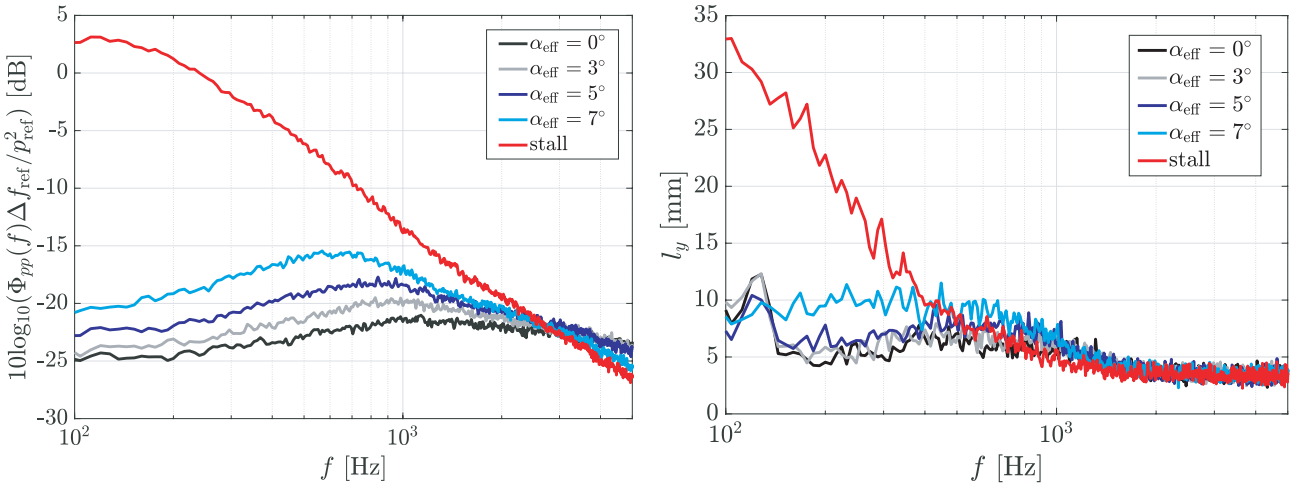

(a) Wall-pressure fluctuations

(b) Spanwise correlation length

Figure 7 – PSD of the WPFs and spanwise correlation length at x/c = 0.97 in the suction side for different angles of attack for Re_c = 6×10^5 and for no inflow turbulence. Reference values: p_{ref} = 1 Pa, Δf_{ref} = 1 Hz.

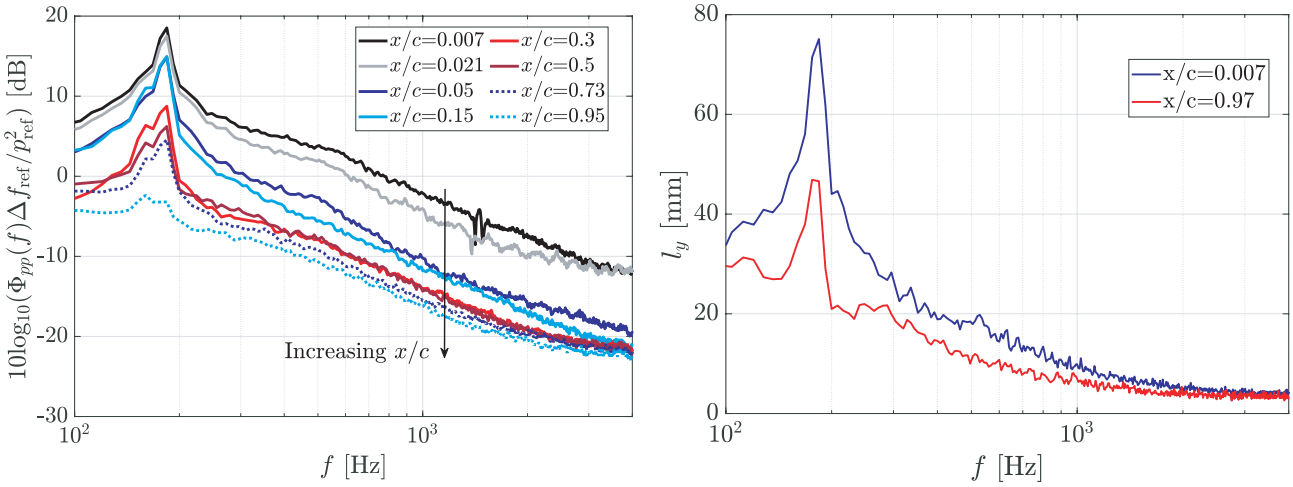

(a) Wall-pressure fluctuations

(b) Spanwise correlation length

Figure 8 – PSD of the WPFs and spanwise correlation length for the case of inflow turbulence generated by a rod for different chordwise positions for Re_c = 4.8×10^5 and α_{eff} = 0°. Reference values: p_{ref} = 1 Pa, Δf_{ref} = 1 Hz.

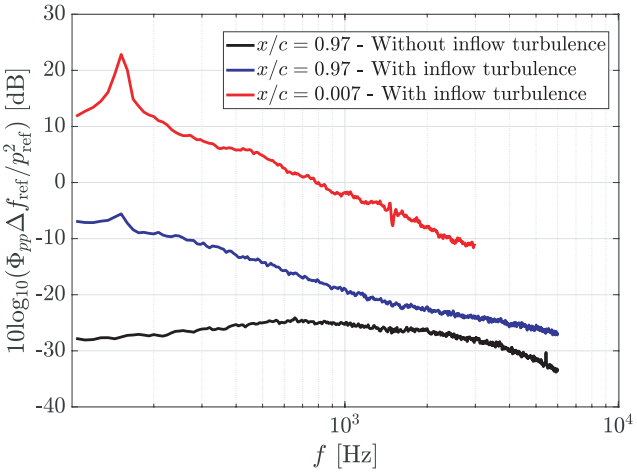

Figure 9 – PSD of the WPFs for the cases without inflow turbulence and with inflow turbulence generated by the rod for different chordwise positions for Re_c = 4×10^5 and α_{eff} = 0°. Reference values: p_{ref} = 1 Pa, Δf_{ref} = 1 Hz.

Figure 9 compares the WPF spectral levels at x/c = 0.97 for the cases without inflow turbulence and with inflow turbulence generated by the rod. The WPF spectrum at $x/c = 0.007$ for the case with inflow turbulence is also shown. From this figure, it is evident that the spectral level at x/c = 0.97 for low frequencies increases considerably when the inflow is turbulent. However, even though the low-frequency energy content of the WPF at the TE increased with the inflow turbulence, the WPFs at the LE are still approximately 16 dB higher (at f = 304 Hz). This observation suggests that the LE is the dominant noise source for low frequencies, which is confirmed in Section 4.2.3. Furthermore, the WPF level also increases for high frequencies when the inflow is turbulent. This increase might have an affect on the TE radiated noise, as discussed by Botero-Bolivar et al. [13].

4.2 Far-Field Noise

4.2.1 Trailing-Edge noise

Figure 10 shows the PSD of the TE noise measured for different Reynolds numbers for α_{eff} = 0°. G_{pp} is the one-sided PSD of the far-field radiated noise. These measurements were performed without inflow turbulence. The TE noise is shown for frequencies where the background noise is not dominant. As expected, the radiated noise level increases with the Reynolds number; see Fig. 10a. The scaling of the TE noise level with the velocity is verified in Figs. 10b and 10c. The x-axis is shown as the Strouhal number based on the boundary layer thickness at the TE determined from XFOIL. It is clear from Figs. 10b and 10c that the TE noise level scales the best with the velocity to the power three. According to Glegg and Devenport [3], the TE noise should scale with the velocity to the power five. The reason why the TE noise scales with a velocity to the power three instead of five is unknown. In Fig. 10a, a hump is observed in the high-frequency range, mainly for high Reynolds numbers, and is shifted to higher frequencies as the Reynolds number increases. We believe that this hump is due to the blunt TE of the NACA 0008, which generates a turbulent vortex street, resulting in a peak or hump in the noise spectrum [33]. According to Brooks and Hodgson [34], blunt TE noise is observed for a Strouhal number based on the TE thickness $ft/U_\infty \approx 0.1$, where t is the TE thickness, which for this study t = 1 mm. By scaling the TE noise level with a velocity to the power three and nondimensionalizing the frequency as ft/U_∞, the hump is observed at $ft/U_\infty \approx 0.09$. Thus, this hump is most probably due to the blunt TE. The hump becomes more evident for high Reynolds numbers because, as the velocity increases, the boundary layer becomes thinner and more comparable to the airfoil TE thickness.

Figure 11 shows the TE noise measured for two Reynolds numbers for different angles of attack. Positive angles of attack indicate that the airfoil suction side was towards the microphone array, whereas negative angles of attack indicate that the pressure side was towards the microphone array. The angle of attack slightly influences the radiated TE noise. This tendency is observed for both

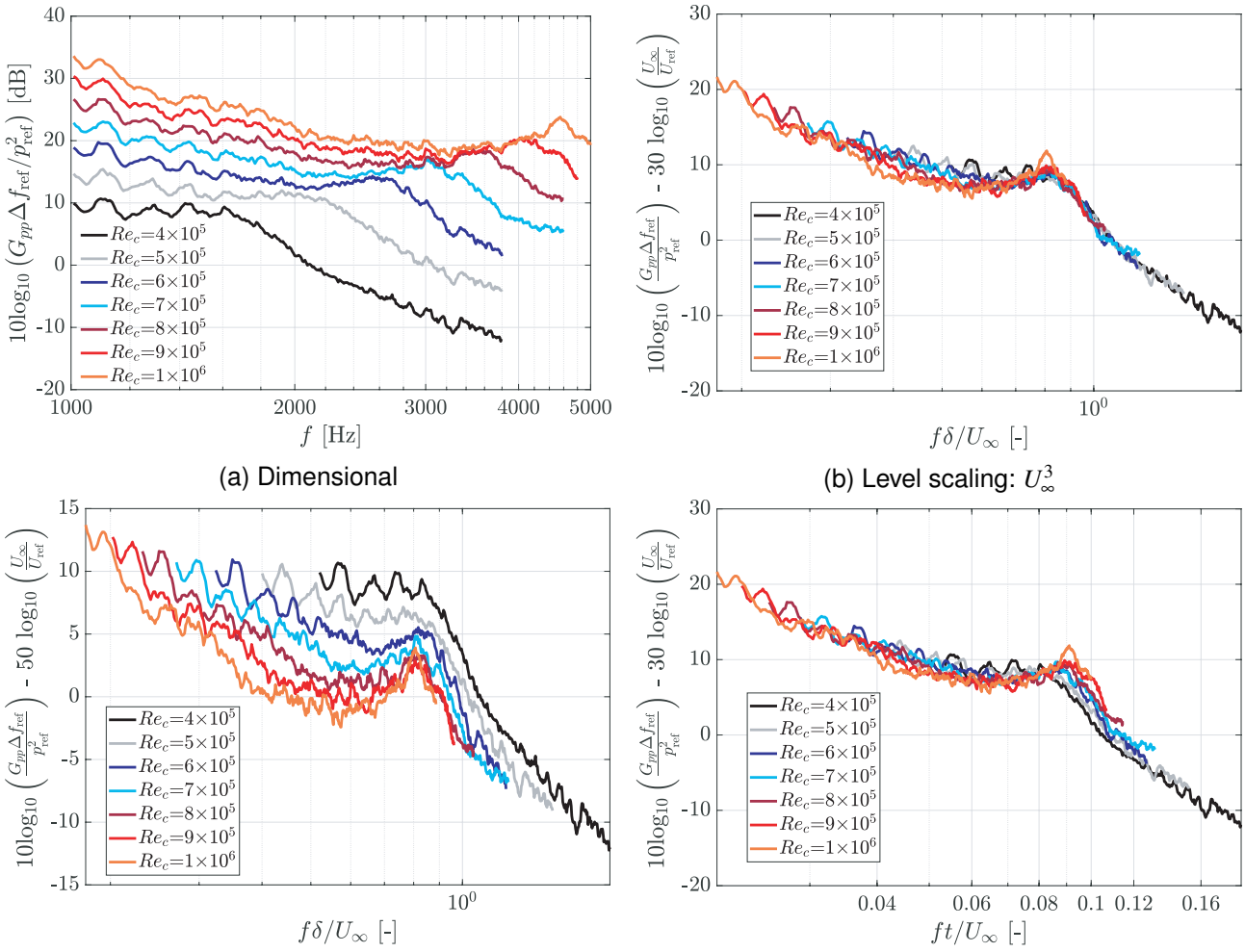

(a) Dimensional

(b) Level scaling: U_∞^3

(c) Level scaling: U_∞^5

(d) Frequency scaling: airfoil TE thickness

Figure 10 – PSD of the TE far-field noise for different Reynolds numbers and $\alpha_{\mathrm{eff}} = 0°$. Tripping device installed at x/c = 0.05. Reference values: p_{ref} = 20 μPa, Δf_{ref} = 1 Hz, U_{ref} = 20 m/s.

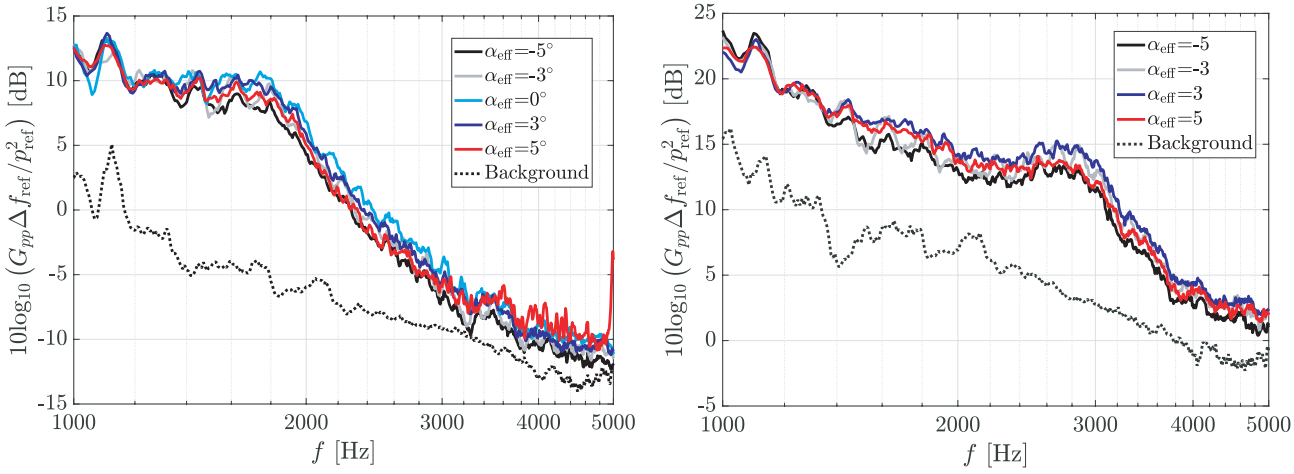

(a) Re_c = 4×10^5

(b) Re_c = 6×10^5

Figure 11 – PSD of the TE far-field noise for two different Reynolds numbers and different angles of attack. Tripping device installed at x/c = 0.05. Reference values: p_{ref} = 20 μPa, Δf_{ref} = 1 Hz.

suction and pressure sides. Hutcheson and Brooks [35] analyzed the angle of attack effect on the TE noise for a NACA 63-215. They observed that the angle of attack mainly affected the TE noise for low frequencies, whereas the noise for high frequencies was seemingly invariant, which agrees with

the observations in this study. The small effect of angle of attack variation on the TE noise for high frequencies is supported by the WPF spectra for the different angles of attack; see Fig. 7. The WPF spectral level for $f > 1000$ Hz is slightly affected by the angle of attack, which is also observed for the TE noise. The hump for high frequencies due to the TE bluntness is also observed for the different angles of attack, mainly for $Re_c = 6\times10^5$.

4.2.2 Leading-Edge Noise

Figure 12 shows the PSD of the LE noise, G_{pp}, generated by the airfoil when subjected to inflow turbulence generated by a rod for different Reynolds numbers. The measured noise is shown for frequencies where the background noise is not dominant. As expected, the LE noise increases with the Reynolds number. Figure 12 also shows the normalized LE noise following the nondimensionalization presented in Fig. 14.6 in [3], where r_e is the observer radius. The curves overlap considerably well in the entire frequency range for the different Reynolds numbers. Noteworthy is that the LE noise is also scaling with a velocity to the power three ($u_{rms} \sim U_\infty$), as also observed for the TE noise.

4.2.3 Leading- and Trailing-Edge Noise Comparison

Figure 13 shows the source maps for the case with inflow turbulence. From this figure, it is clear that the noise generated by the airfoil LE interacting with the inflow turbulence generated by the rod, i.e., LE noise, is dominant for frequencies up to 2520 Hz. From Fig. 9, it is observed that the WPF energy content at the TE for the measurements with inflow turbulence increased for low frequencies, which probably results in an increase of the TE noise. However, Fig. 13 clearly shows that the LE noise is the dominant noise source. Thus, even though the WPF levels at the TE increase with inflow turbulence, the LE noise is still the dominant noise source for low and mid frequencies. The TE noise is not evaluated for the case with inflow turbulence because this noise source is not observed in the source maps.

Figure 14 shows the leading- and trailing-edge noise for different Reynolds numbers. It is important to highlight that the TE noise was measured without inflow turbulence. The effect of the inflow turbulence on the TE noise is still not well understood, as discussed in [13], but it is clear from the results shown in Fig. 13 that the LE noise is dominant for frequencies up to 2520 Hz. Assuming that the inflow turbulence does not affect the TE noise, we can clearly see that the LE noise dominates the far-field noise, mainly for low and mid frequencies where a difference of up to 18 dB (f = 1008 Hz and $Re_c = 4\times10^5$) is observed. Assuming that the LE noise decay for high frequencies follows the same decay as for lower frequencies, the TE noise becomes relevant for high frequencies.

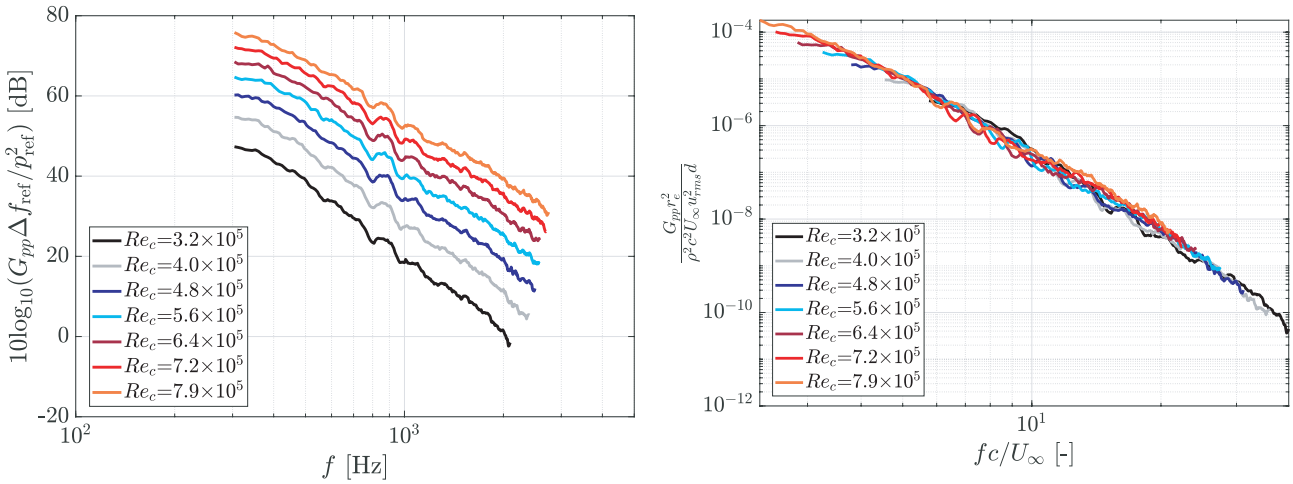

(a) Dimensional

(b) Nondimensional

Figure 12 – PSD of the LE far-field noise for different Reynolds numbers and $\alpha_{\text{eff}} = 0°$. Reference values: p_{ref} = 20 μPa, Δf_{ref} = 1 Hz.

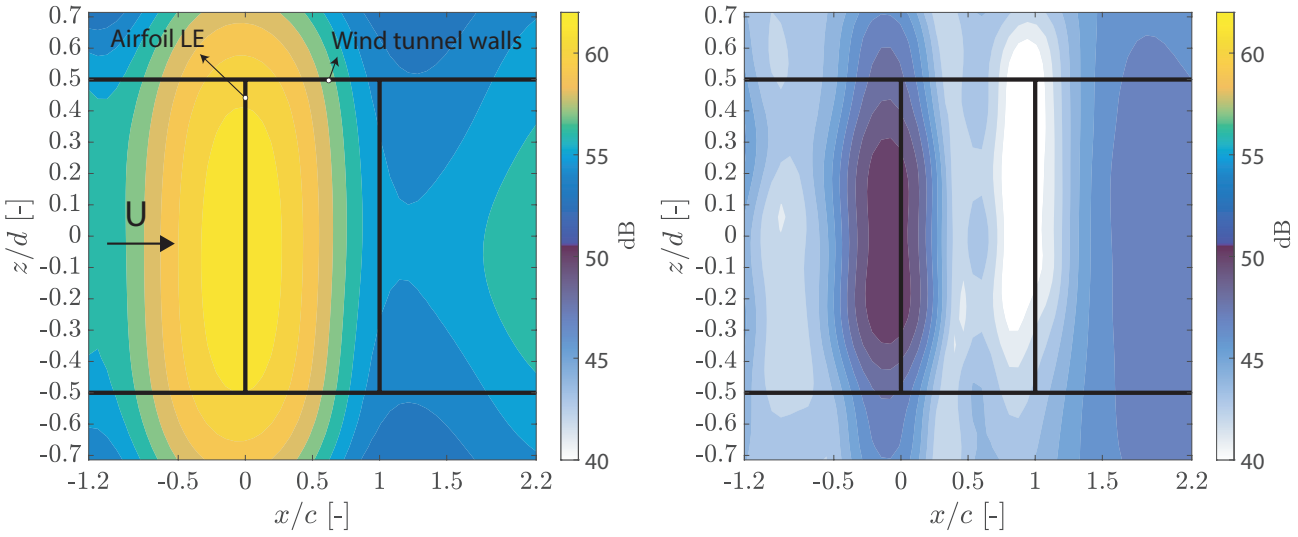

(a) 1260 Hz (b) 2520 Hz

Figure 13 – 1/3-octave band source maps for the with inflow turbulence for two center frequencies. Reference values: p_{ref} = 20 µPa, Δf_{ref} = 1 Hz.

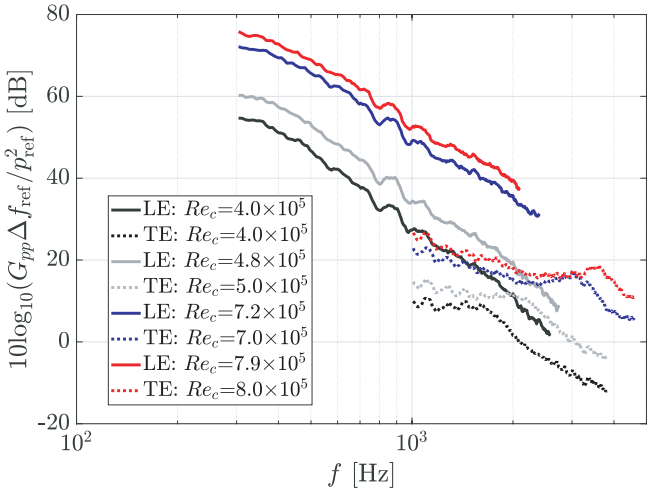

Figure 14 – Leading- and trailing-edge far-field noise comparison for different Reynolds numbers. Reference values: p_{ref} = 20 µPa, Δf_{ref} = 1 Hz.

5. Conclusions

This paper presents the aerodynamic and aeroacoustic characterization of a NACA 0008 airfoil. For the aerodynamic characterization, the pressure and lift coefficients and the boundary layer parameters at the airfoil TE were determined experimentally and compared with XFOIL results. The XFOIL simulations agree reasonably well with the experimental results, indicating that this simulation tool can be used to estimate the aerodynamic characteristics of the NACA 0008. This is an important conclusion because the aerodynamic parameters from XFOIL can be used to estimate the TE far-field noise when used in combination with Amiet's theory [4] coupled with a wall-pressure spectrum model [25; 26; 27].

The aeroacoustic characterization was carried out by measuring the WPFs at different chordwise positions and the far-field noise for the cases without inflow turbulence and with inflow turbulence generated by a rod. For the case without inflow turbulence, the TE noise is the dominant noise source. The TE noise is a combination of blunt TE noise and turbulent boundary layer TE noise. The TE noise scales with the third power of the free-stream velocity, whereas the WPFs at x/c = 0.97 scales with the velocity to the power two. The low-frequency energy content of the WPFs at x/c = 0.97 increases as the angle of attack increases, presenting a considerable growth at stall condition. For high frequencies, the WPFs and the TE noise are slightly influenced by the angle of attack. For the case with inflow turbulence, the energy content of the WPFs increases considerably for all chordwise positions, mainly in the low-frequency range, due to the turbulent inflow. The energy level of the WPFs close to the LE is the highest, with a difference of approximately 16 dB (f = 304 Hz) to the energy levels of the WPFs close to the TE. The LE noise is the dominant noise source for frequencies up to approximately 2.5 kHz for Re_c = 4×10^5. The TE noise becomes comparable to the LE noise for high frequencies (> 3 kHz for $Re_c = 4 \times 10^5$). The LE noise also scales with the third power of the free-stream velocity.

Funding Sources

Part of this research received financial support from the European Commision through the H2020-MSCA-ITN-209 project zEPHYR (grant agreement No 860101).

Acknowledgments

The authors are grateful to Ing. W. Lette, ir. E. Leusink, S. Wanrooij for their technical support and assistance during the wind tunnel tests. The authors would like to thank TNO and the Maritime Research Institute Netherlands (MARIN), particularly Dr. Johan Bosschers, Dr. Roel Müller, and Dr. Christ de Jong, for the insightful discussions.

6. Corresponding Author Email Address

Contact email address of the corresponding author: f.l.dossantos@utwente.nl

7. Copyright Statement

References

[1] European Parliament, "Directive 2002/49/EC of the European Parliament and of the Council of 25 June 2002 relating to the assessment and management of environmental noise." Official Journal of the European Communities, 2002.

[2] J. L. Davy, K. Burgemeister, and D. Hillman, "Wind turbine sound limits: Current status and recommendations based on mitigating noise annoyance," *Applied Acoustics*, vol. 140, pp. 288–295, 2018.

[3] S. Glegg and W. Devenport, *Aeroacoustics of Low Mach Number Flows*. Academic Press, 2017.

[4] R. Amiet, "Noise due to turbulent flow past a trailing edge," *Journal of Sound and Vibration*, vol. 47, no. 3, pp. 387 – 393, 1976.

[5] S. Oerlemans, P. Sijtsma, and B. Méndez López, "Location and quantification of noise sources on a wind turbine," *Journal of Sound and Vibration*, vol. 299, no. 4, pp. 869–883, 2007.

[6] X. Zhang, "Airframe noise – high lift device noise," *Encyclopedia of Aerospace Engineering*, 2010.

[7] J. Carlton, *Marine Propellers and Propulsion*. Butterworth-Heinemann, 2018.

[8] M. Roger and S. Moreau, "Back-scattering correction and further extensions of amiet's trailing-edge noise model. part 1: theory," *Journal of Sound and Vibration*, vol. 286, no. 3, pp. 477–506, 2005.

[9] R. Amiet, "Acoustic radiation from an airfoil in a turbulent stream," *Journal of Sound and Vibration*, vol. 41, no. 4, pp. 407 – 420, 1975.

[10] S. Moreau and M. Roger, "Competing broadband noise mechanisms in low-speed axial fans," *AIAA Journal*, vol. 45, no. 1, pp. 48–57, 2007.

[11] H. Arbey, *Contribution à l'Étude des Mécanismes de l'Émission Sonore de Profils Aérodynamiques Placés Dans des Écoulements Sains ou Perturbés*. PhD thesis, Univ. Claude Bernard, 1981.

[12] S. Moreau and M. Roger, "Effect of angle of attack and airfoil shape on turbulence-interaction noise," *11th AIAA/CEAS Aeroacoustics Conference*, 2012.

[13] L. Botero-Bolívar, F. dos Santos, L. de Santana, and C. Venner, "The increase of the airfoil trailing edge noise and unsteady surface pressure due to high inflow turbulence," *AIAA AVIATION 2021 FORUM*, 2021.

[14] P. F. Mish and W. J. Devenport, "An experimental investigation of unsteady surface pressure on an airfoil in turbulence—part 1: Effects of mean loading," *Journal of Sound and Vibration*, vol. 296, no. 3, pp. 417–446, 2006.

[15] F. L. dos Santos, L. Botero-Bolívar, C. H. Venner, and L. D. de Santana, "Influence of roughness trips on near- and far-field trailing-edge noise," *AIAA Journal*, 2022. Accepted.

[16] L. de Santana, M. P. Sanders, and C. H. Venner, "The utwente aeroacoustic wind tunnel upgrade," *2018 AIAA/CEAS Aeroacoustics Conference*, 2018. AIAA 2018-3136.

[17] W. von Heesen and M. Höpfer, "Suppression of wind tunnel buffeting by active flow control," *SAE 2004 World Congress & Exhibition*, mar 2004.

[18] F. L. dos Santos, L. Botero-Bolívar, C. H. Venner, and L. D. de Santana, "On the turbulence distortion effects for airfoil leading-edge noise prediction," *28th AIAA/CEAS Aeroacoustics Conference*, 2022.

[19] M. Roger, "Microphone measurements in aeroacoustic installations," educational notes, sto-en-avt-287, S&T organization, 2017.

[20] C. R. Berntsen, "The remote microphone probe for unsteady surface pressure measurement," Master's thesis, University of Notre Dame, 2014.

[21] E. Sarradj, "Optimal planar microphone array arrangements," in *DAGA 2015, Nürnberg*, 2015.

[22] C. Bahr, W. Humphreys, D. Ernst, T. Ahlefeldt, C. Spehr, A. Pereira, Q. Leclere, C. Picard, R. Porteous, D. Moreau, J. Fischer, and C. Doolan, "A comparison of microphone phased array methods applied to the study of airframe noise in wind tunnel testing," in *23rd AIAA/CEAS Aeroacoustics Conference*, 2017. AIAA 2017-3718.

[23] E. Sarradj, G. Herold, P. Sijtsma, R. Merino-Martinez, A. Malgoezar, M. Snellen, T. Geyer, C. Bahr, R. Porteous, D. Moreau, and C. Doolan, "A microphone array method benchmarking exercise using synthesized input data," in *23rd AIAA/CEAS Aeroacoustics Conference*, 2017. AIAA 2017-3719.

[24] T. Brooks and W. Humphreys, "Effect of directional array size on the measurement of airframe noise components," in *5th AIAA Aeroacoustics Conference*, 1999. AIAA 99-1958.

[25] D. M. Chase, "Modeling the wavevector-frequency spectrum of turbulent boundary layer wall pressure," *Journal of sound and Vibration*, vol. 70, no. 1, pp. 29–67, 1980.

[26] M. Goody, "Empirical spectral model of surface pressure fluctuations," *AIAA journal*, vol. 42, no. 9, pp. 1788–1794, 2004.

[27] R. R. Parchen, *Progress report DRAW: A prediction scheme for trailing edge noise based on detailed boundary layer characteristics*. TNO Institute of Applied Physics, 1998.

[28] O. Stalnov, P. Chaitanya, and P. F. Joseph, "Towards a non-empirical trailing edge noise prediction model," *Journal of Sound and Vibration*, vol. 372, pp. 50–68, 2016.

[29] M. Drela, "Xfoil: An analysis and design system for low reynolds number airfoils," *Low Reynolds Number Aerodynamics*, vol. 54, pp. 1–12, 1989.

[30] M. Drela and M. B. Giles, "Viscous-inviscid analysis of transonic and low reynolds number airfoils," *AIAA Journal*, vol. 25, no. 10, pp. 1347–1355, 1987.

[31] T. F. Brooks, D. S. Pope, and M. A. Marcolini, "Airfoil self-noise and prediction," Tech. Rep. NASA Reference Publication 1218, NASA, 1989.

[32] D. Coles, "The law of the wake in the turbulent boundary layer," *Journal of Fluid Mechanics*, vol. 1, no. 2, pp. 191—226, 1956.

[33] C. H. Hansen, C. J. Doolan, and K. L. Hansen, *Wind Farm Noise: Measurement, Assessment and Control*. John Wiley & Sons Ltd, UK, 2017.

[34] T. Brooks and T. Hodgson, "Trailing edge noise prediction from measured surface pressures," *Journal of Sound and Vibration*, vol. 78, no. 1, pp. 69–117, 1981.

[35] F. Hutcheson and T. Brooks, "Effects of angle of attack and velocity on trailing edge noise," *42nd AIAA Aerospace Sciences Meeting and Exhibit*, 2004. AIAA 2004-1031.